Development of an Active Cerebrovascular Autoregulation Model Using Representation Learning: A Proof of Concept Study With Experimental Data

Bavo Kempen, MSc [‡§], **Samuel Klein, MD, PhD** [‖], **Veerle De Sloovere, MD** [¶], **Maarten De Vos, Ir, PhD** [§#*], **Bart Depreitere, MD, PhD** [‡**]

[‡]Department of Neurosciences, Experimental Neurosurgery and Neuroanatomy, KU Leuven, Leuven, Belgium; [§]Department of Electrical Engineering (ESAT), STADIUS Center for Dynamical Systems, Signal Processing and Data Analytics, KU Leuven, Leuven, Belgium; [‖]Neurosurgical Center Limburg, Limburg, Belgium; [¶]Department of Anesthesiology, University Hospitals Leuven, Leuven, Belgium; [#]Department of Development and Regeneration, Woman and Child, KU Leuven, Leuven, Belgium; **Department of Neurosurgery, University Hospitals Leuven, Leuven, Belgium

Presented as an oral abstract at the 2024 Annual BrainIT meeting, Glasgow, Scotland on May 24, 2024 and at the 2024 International Neurotrauma Society (INTS) conference, Cambridge, England on September 4th, 2024.

*Bart Depreitere and Maarten De Vos contributed equally to this work.

Correspondence: Bavo Kempen, MSc, Department of Neurosciences, Experimental Neurosurgery and Neuroanatomy, KU Leuven, Herestraat 49 – Box 503, Leuven 3000, Belgium. Email: bavo.kempen@kuleuven.be; Bart Depreitere, MD, PhD, Department of Neurosurgery, University Hospitals Leuven, Herestraat 49 – Box 7003, Leuven 3000, Belgium. Email: bart.depreitere@uzleuven.be

Received, June 06, 2024; **Accepted,** October 27, 2024; **Published Online,** January 8, 2025.

Neurosurgery 00:1–10, 2025 https://doi.org/10.1227/neu.0000000000003321

© Congress of Neurological Surgeons 2025. All rights reserved.

BACKGROUND AND OBJECTIVES: It remains a challenge to monitor cerebrovascular autoregulation (CA) reliably and dynamically in an intensive care unit. The objective was to build a proof-of-concept active CA model exploiting advances in representation learning and the full complexity of the arterial blood pressure (ABP) and intracranial pressure (ICP) signal and outperform the pressure reactivity index (PRx).

METHODS: A porcine cranial window CA data set (n = 20) was used. ABP and ICP signals were preprocessed and downsampled to 20 Hz. Quadriphasic CA state labels were assigned to each piglet's CA curve and projected on their preprocessed ABP and ICP time series. Windowed ABP and ICP segments of 300 seconds, reflecting active CA, were used to optimize a neural network to reconstruct its own input. Reconstruction error of ABP and ICP were compared between active CA and inactive CA, and assessed together with PRx over quadriphasic CA states.

RESULTS: The study confirmed that the optimized model achieved stellar reconstruction quality of ABP and ICP segments that derived from active CA while reconstruction quality deteriorated for segments that came from inactive CA. ABP and ICP reconstruction errors steadily increased concurrently with cerebral blood flow deviation from baseline. A significant interaction between variable and CA state showed that the model captured the differential behavior of CA with increasing vs decreasing cerebral perfusion pressures and offered improved discriminative ability regarding PRx.

CONCLUSION: The present work showed that an active CA model can be built using advanced representation learning and the full complexity of 300-second ABP and ICP segments. On assessment in an experimental data set, relevant CA state information was present in both lower and higher frequencies of ABP and ICP. Improved discriminative ability between CA states was attained regarding PRx, which focuses only on slow-wave ABP and ICP information.

KEY WORDS: Arterial blood pressure, Cerebrovascular autoregulation, Intracranial pressure, Machine learning, Pressure reactivity index, Representation learning

ABBREVIATIONS: CA, cerebrovascular autoregulation; **CPP,** cerebral perfusion pressures; **HiCA,** high inactive CA; **HPaCA,** hypertensive high partially active CA; **LDF,** laser Doppler flowmetry; **LiCA,** hypotensive low inactive CA; **LLA,** lower limit of autoregulation; **LogMSE,** log transformed mean squared reconstruction error; **PRx,** Pressure reactivity index; **TBI,** traumatic brain injury; **ULA,** upper limit of autoregulation.

Supplemental digital content is available for this article at neurosurgery-online.com.

© Congress of Neurological Surgeons 2025. Unauthorized reproduction of this article is prohibited.

Cerebrovascular autoregulation (CA) is a homeostatic physiological mechanism that ensures an adequate cerebral blood flow (CBF) over a varying range of cerebral perfusion pressures (CPP).[1-4] CPP reflects the pressure gradient between arterial blood pressure (ABP) and intracranial pressure (ICP) (CPP = ABP-ICP). The crucial mechanism driving CA is myogenic: Changes in intraluminal pressure and flow are reflected in changes to arteriolar vessel tone and, hence, in cerebrovascular resistance.[5-7] However, the capacity of CA to adjust arteriolar vessel diameters in response to CPP decreases or increases is limited.[6,8]

Lassen[1] introduced the seminal triphasic CA curve by plotting CBF (*y*-axis) against CPP (*x*-axis). A plateau of stable CBF emerged over a wide range of CPP values, edged by a lower and upper limit of autoregulation (LLA and ULA), which indicate the transition points from active to inactive CA. Recent experimental work showed that the CA curve was quadriphasic, with 2 ULAs.[6,8] The transition from ULA1 to ULA2 represents a gradual exhaustion of CA. Although the static representation of CA remains useful to study the mechanism, its clinical utility is severely limited due to (1) intraindividual and interindividual LLA and ULA(s) variation reflecting the dynamic and gradual nature of CA impairment and (2) a lack of reliable CBF monitors.[4,6,8-11]

In traumatic brain injury (TBI), CA can be dynamically impaired.[12-16] Knowledge of CA capacity could aide to steer blood pressure out of hypoperfusion and hyperperfusion ranges. Indirect correlation-based CA indices exist that use a CBF surrogate and ABP to capture CA capacity dynamically.[17] Positive or negative correlations are interpreted as inactive or active CA, respectively. Pressure reactivity index (PRx) is computed as the moving correlation coefficient between 30 consecutive 10 second averages of ICP and ABP, to model the slow-wave (≤0.05 Hz) arterial transmission to the brain, ie, myogenic cerebrovascular resistance changes.[17-20] Numerous drawbacks exist to using a simple correlation coefficient to model a complex, multifaceted biological mechanism.[4] Relevant CA higher-frequency components, eg, Mayer waves (0.1 Hz), cardiac cycle (1-1.3 Hz), and ICP pulse morphology information, among others, are ignored.[21-28] Modeling the full complexity of ABP and ICP could aid in delineating active from inactive CA dynamically.

Adoption of advanced machine learning methods to directly model CA from multivariate physiological time series is lacking. A data-driven machine learning approach seems appropriate to model CA directly from the full complexity of ABP and ICP. Sequentially connected encoder and decoder neural network architectures excel at modeling multivariate nonlinear interactions by optimizing the encoder and decoder network concurrently. The encoder network learns to project the input data to an optimal latent representation while the decoder network learns to reconstruct the original input data from the latter latent representation. This method has been widely adopted in the field of anomaly detection. Unsupervised encoder-decoder anomaly detection methods were successful in modeling arrhythmia detection from electrocardiography, among others.[29-35] Anomaly detection involves identifying observations in the data that deviate from the learned concept of normal behavior, often generated by distinct underlying mechanisms.[36] Similarly, active and inactive CA can be considered as normal and abnormal behavior, respectively.

The aim of this work was to build a proof-of-concept dynamic CA monitor using representation learning and the full complexity of the ABP and ICP signal. An encoder-decoder neural network architecture is optimized to reconstruct its own multivariate ABP and ICP input, which reflected an active CA state. Consequently, the model will have learned a generalized active CA representation, ie, normal behavior. It is hypothesized that distinct individual signal components and interactions present within and between the ABP and ICP signal characterize the active and inactive CA states. The reconstruction performance of the encoder-decoder model should be worse when the input is governed by inactive CA, ie, abnormal behavior. An increase in reconstruction error of the ABP and ICP input has the potential to signal when a patient experiences failing CA. In sum, the encoder-decoder model is expected to (1) adequately reconstruct ABP and ICP segments governed by active CA, with deteriorating performance on ABP and ICP input segments governed by inactive CA, and (2) improve the ability to dynamically discriminate between active and inactive CA regarding PRx.

METHODS

Data Set

The unique data set used for this study derives from a porcine-closed cranial window model previously developed for the study of CA.[6,8] In brief, twenty 6-week-old male piglets (domestic swine) were non-pharmacologically induced with hypotension or hypertension by gradually inflating a balloon catheter (LeMaitre embolectomy catheter® 1601-54, LeMaitre Vascular) in the inferior vena cava or abdominal aorta, respectively (**Supplemental Digital Content 1** [http://links.lww.com/NEU/E623]). ABP was monitored through an arterial line placed in the left femoral artery. An intraparenchymal ICP probe (Neurovent®-PTO, Raumedic AG Muenchenberg) and laser Doppler flowmetry (LDF) probe (Moor VMS-LDF1 with VP14-CBF probe, Moor Instruments) were placed in two 3-4 mm burr holes behind the coronal suture over the right hemisphere.[6,8] The ICP probe perforated the dura, while the LDF probe did not. Meanwhile, ICM+ software (Cambridge University) was used to store ABP (100 Hz), ICP (100 Hz), and LDF (500 Hz). LDF served as a direct measurement of CBF, validated in previous work using CBF Flux computed from pial arterioles' diameter and red blood cell velocity.[6,8] Animal experimentation in the preceding data gathering study complied with the European Directive 2010/63/EU on the protection of animals used for scientific purposes and was performed under veterinary supervision adhering to the guidelines imposed by the Ethical Committee.[6,8]

First, the quadriphasic CA definition was used to assign the CA state labels per piglet.[6] A segmented regression was computed per piglet to derive the LLA and ULAs reflecting a change in CA state (Figure 1A). No reliable breakpoints could be computed for 4 of 20 piglets, which led to their immediate exclusion from the study, resulting in a final data set of

© Congress of Neurological Surgeons 2025. Unauthorized reproduction of this article is prohibited.

16 piglets ($n_{hypotensive}$ = 7). Henceforth, the quadriphasic CA state labels will be defined as follows: active CA, low ABP inactive CA = LiCA, high ABP partially active CA = HPaCA, and high ABP inactive CA = HiCA.

Second, raw ABP and ICP time series were extracted from the ICM+.hdf5 data format.[37] Extreme values were filtered out using absolute values (ABP >300 mm Hg; ABP <10 mm Hg; ICP < −5 mm Hg) and a z-score filter ($\mu_{Signal} \pm 3^{*}\sigma_{Signal}$) per piglet. No data imputation was performed. The CA transition points determined per piglet (Figure 1A) were used to project the CA state onto the corresponding extracted ABP and ICP time series data (Figure 1B), followed by downsampling from 100 Hz to 20 Hz with a 10 Hz low-pass Butterworth filter of the fifth order.[38,39]

Model Architecture

Model architecture consisted of an encoder and decoder model. The encoder model used TimesBlocks[35] (Figure 2), a temporal 2-dimensional variation modelling technique which achieved stellar performance on unsupervised multivariate time series anomaly detection benchmarks, among other tasks. The complete explanation and rationale of TimesBlocks can be found in the study by Wu et al[35] (2023) with accompanying illustrations and code. A fully connected layer, a series of linear transformations, served as decoder network.

Model Optimization

The model is optimized to reconstruct its own input (ie, active CA ABP and ICP time series) and as such is forced to learn a generalizable representation of said input. Sixteen piglets were subdivided in a train (n = 12), validation (n = 2), and test (n = 2) data sets after a so called cross-validation procedure. The complete optimization and evaluation procedure is provided in **Supplemental Digital Content 2** (http://links.lww.com/NEU/E624). In essence, 8 unique permutations of the data set were created where the available 16 piglets were randomly assigned to the train, validation, and test data set, stratified on ABP manipulation (hypotension vs hypertension). Eight models were optimized and tested with the corresponding unique data subsets to ensure robustness of the results. The train data set was used to optimize the model, and the validation data set served as intermediate check to ensure the generalizability. The test data set was used to independently assess the final performance of each model after convergence. Each training and validation data set consisted of concurrent ABP and ICP segments of 300 seconds (20 Hz) extracted from data that belonged to the active CA state with a 99 % overlap. For the test data set, 300 second (20 Hz) segments were extracted from all CA states without overlap. Model training, validation, and testing was performed with Python 3.9.16 (Python Software Foundation).[40,41]

Model Performance Assessment

Model performance was assessed both qualitatively and quantitatively for all CA states. The qualitative check was performed by randomly sampling and visualizing ABP and ICP test data set segment reconstructions with its respective original input. Quantitative assessment consisted of evaluating ABP and ICP reconstruction error trends over time, and over CPP in comparison with the average reconstruction error under active CA and regarding baseline LDF. Linear mixed effect models were used to assess whether (1) CA state affected PRx, or (2) CA state affected ABP and ICP reconstruction errors.[42] In linear mixed effect model (1) PRx served as the dependent variable (DV) and CA state as the

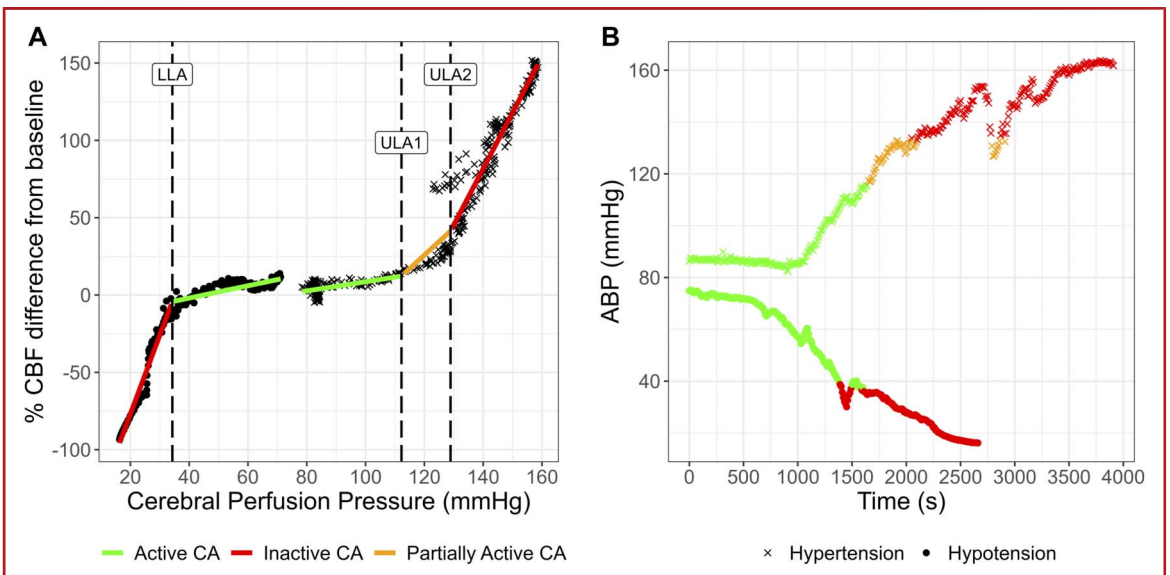


FIGURE 1. *An example of CA state projection on ABP time series.* **A**, *The quadriphasic curve constructed from a hypotension and hypertension piglet experiment data set. Cerebral perfusion pressure was plotted against the percentage change of laser Doppler flowmetry from baseline values before ABP manipulation. LLA and ULA1 and ULA2 were computed using segmented regression with 1 and 2 breakpoints, respectively.*[6,8] **B**, *Projection of CA states determined in* **A** *on the respective hypotension and hypertension experiment piglets' ABP time series. The time series data used in this study were annotated per piglet with the respective CA states accordingly. ABP, arterial blood pressure; Active CA, active cerebrovascular autoregulation; CBF, cerebral blood flow; LLA, lower limit of autoregulation; ULA, upper limits of autoregulation.*

© Congress of Neurological Surgeons 2025. Unauthorized reproduction of this article is prohibited.

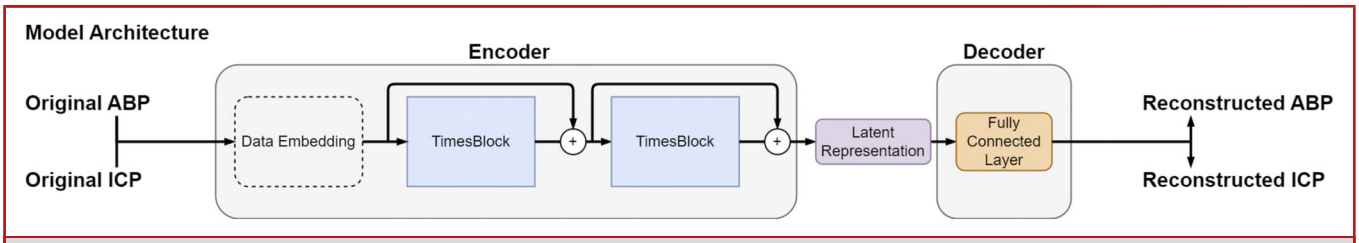


FIGURE 2. *Model architecture. The architecture consisted of a sequentially connected encoder and decoder neural network, which was input with 300 seconds of concurrent ABP and ICP segments sampled at 20 Hz. Model is optimized to reconstruct the original ABP and ICP input segments using mean squared error loss. The encoder network comprised a data embedding layer and 2 residually connected TimesBlocks,[35] each selective for the top 8 frequencies. Inception blocks consisted of 6 kernels with 0.1 dropout. Activation functions used were Gaussian Error Linear Units. Latent representation comprised 8 dimensions. A simple linear feed forward layer reconstructs the input data from the latent representation in the decoder network. The model comprised 73 522 trainable parameters and was optimized on a single NVIDIA V100 GPU for 100 epochs with a batch size of 32 and the adaptive moment estimation (Adam) optimizer with a starting learning rate of 0.0001. Model training was halted when the validation loss did not decrease for 5 consecutive epochs. ABP, arterial blood pressure; ICP, intracranial pressure.*

independent variable (IV), with a by-piglet random intercept and slope for CA state. In linear mixed effect model (2), log transformed mean squared reconstruction error (LogMSE) served as the DV with a main effect of CA state, variable (ie, ABP, ICP), and their interaction as IV, with by-piglet, cross-validation fold random intercepts and slopes for variable and CA state. Detailed linear mixed effect model specifications are provided in **Supplemental Digital Content 3** (http://links.lww.com/NEU/E625) and **Supplemental Digital Content 4** (http://links.lww.com/NEU/E626). If CA state was a significant predictor for (1) PRx (ie, main effect) or (2) reconstruction error (ie, interaction with variable), the effect of CA state (eg, Active CA vs LiCA) was further investigated using pairwise comparisons (asymptotic z-test), corrected with Holm[43]-Bonferroni for multiple comparisons. Secondary analyses and visualizations were performed in R (R Foundation).[44-46]

RESULTS

The trained model was evaluated on an independent test data set that consisted of unseen hypotension and hypertension experimental data. To evaluate PRx performance, the same unique hypotension and hypertension data were used. The distribution of test segments evaluated per CA class was as follows: (1) PRx: active CA = 86.57%; LiCA = 2.43%; HPaCA = 6.09%; HiCA = 4.91% and (2) our model: active CA = 87.74%; LiCA = 1.92%; HPaCA = 4.09%; HiCA = 6.25%.

Model Performance

To initially assess reconstruction performance of the optimized models, a qualitative ABP and ICP signal reconstruction inspection was warranted. A zoomed 10 seconds from a total of 300-second view is provided here (Figure 3). The full respective traces can be found in **Supplemental Digital Content 5** (http://links.lww.com/NEU/E627), **Supplemental Digital Content 6** (http://links.lww.com/NEU/E628), **Supplemental Digital Content 7** (http://links.lww.com/NEU/E629), and **Supplemental Digital Content 8** (http://links.lww.com/NEU/E630).

ABP and ICP reconstruction error increased over time when approaching inactive CA states (LiCA, HPaCA), visualized by centering the onset of inactive CA as time point zero per piglet (Figure 4). ABP and ICP reconstruction error increases occurred concurrently with an increase or decrease in LDF. Similarly, ABP and ICP reconstruction error increased concurrently with LDF when plotted against CPP (Figure 5A) and followed LDF percentage decrease/increase more closely than PRx on both the low and high CPP side (Figure 5B).

Statistical analyses were performed for the developed model's ABP and ICP LogMSE (Figure 6A) and PRx (Figure 6B) separately. A significant main effect of CA state (P < 1e-04), variable (P < 1e-04), and their interaction (P = .0001) emerged to predict LogMSE. Further pairwise comparisons (**Supplemental Digital Content 9** [http://links.lww.com/NEU/E631]) revealed that (1) ABP active CA reconstruction error was significantly lower than inactive CA reconstruction error ($Est._{ActiveCA\text{-}HPaCA} = -0.5193 \pm 0.1975$, P = .0343; $Est._{LiCA\text{-}ActiveCA} = 0.9968 \pm 0.2605$, P = .0009; $Est._{ActiveCA\text{-}HiCA} = -1.3614 \pm 0.1594$, P < 1e-04), and (2) ICP active CA reconstruction error was significantly lower than fully inactive CA reconstruction error ($Est._{LiCA\text{-}ActiveCA} = 2.4006 \pm 0.2605$, P < 1e-04; $Est._{ActiveCA\text{-}HiCA} = -0.9601 \pm 0.1594$, P < 1e-04), but not HPaCA ($Est._{ActiveCA\text{-}HPaCA} = -0.0288 \pm 0.1975$, P = .8839) (Figure 6A). ICP reconstruction error increased more than ABP reconstruction error in LiCA regarding active CA while the opposite holds true in HPaCA and HiCA. In the second analysis, PRx served as the DV and only CA state as IV. CA state was a significant predictor of PRx value (P = .0122). Pairwise comparisons (**Supplemental Digital Content 10** [http://links.lww.com/NEU/E632]) of the fixed CA state effect on PRx revealed that PRx governed by active CA was on average significantly lower than PRx governed by HiCA ($Est._{ActiveCA\text{-}HiCA} = -0.4183 \pm 0.1382$, P = .0148), but not LiCA nor HPaCA (Figure 6B).

DISCUSSION

This study using experimental CA data from a cranial window piglet model demonstrated that a machine learning approach is

© Congress of Neurological Surgeons 2025. Unauthorized reproduction of this article is prohibited.

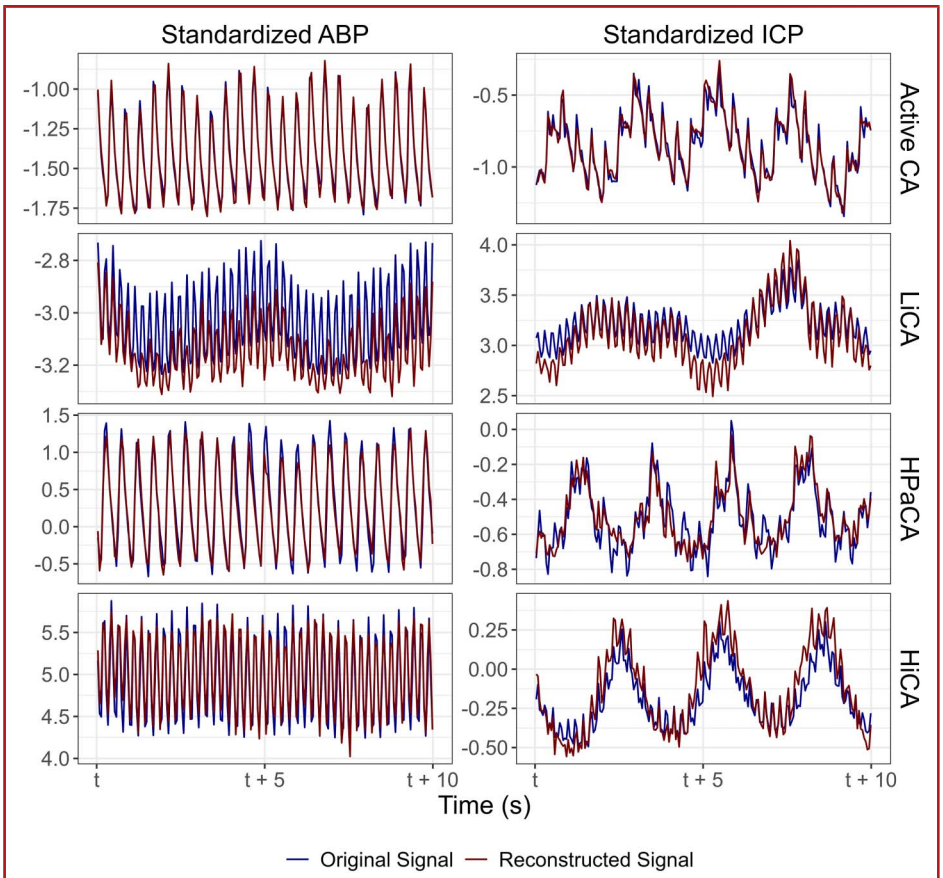


FIGURE 3. *Original ABP and ICP input traces and respective reconstructions from the test data set. Left and right figures per row concern concurrent standardized ABP and ICP traces, respectively. Here, a zoomed 10 seconds from a total of 300-second view is provided. Row 1 to 4 displays an ABP and ICP trace (blue), and its reconstruction (red) randomly sampled from the active CA state, LiCA state, HPaCA state, and HiCA state, respectively. ABP, arterial blood pressure; active CA, active cerebrovascular autoregulation; HiCA, high inactive CA; HPaCA, hypertensive high partially active CA; ICP, intracranial pressure; LiCA, hypotensive low inactive CA.*

suitable to delineate active CA from inactive CA. The state-of-the-art deep representation learning architecture, using TimesBlocks,[35] was used to successfully learn an active CA representation from 300-second concurrent ABP and ICP segments sampled at 20 Hz. The model converged to a generalized representation of active CA based on the multivariate ABP and ICP input data, which significantly differed from inactive CA as shown by the increased reconstruction errors.

Representation learning models are a powerful tool to extract meaningful information from complex multivariate input data.[30-35,47] The proposed model architecture had the capacity to adequately learn an active CA representation from ABP and ICP, which allowed it to qualitatively reconstruct test data governed by active CA, with negligible quantitative reconstruction error. As hypothesized, reconstruction error of ABP and ICP governed by inactive CA was significantly higher than the reconstruction error of ABP and ICP governed by active CA. Interestingly, the reconstruction performance displayed a significant interaction between quadriphasic CA state and variable, allowing to differentiate between hypotensive and hypertensive inactive CA. The model's invariance to absolute signal changes excludes that absolute increases or decreases in ABP or ICP (in mm Hg) caused said interaction. Instead, our model may have learned multivariate active CA frequency, amplitude, and phase representation.

PRx seemed to follow the expected trend with a negative median correlation under active CA and a positive median correlation for inactive CA (Figure 6B). However, large overlaps between CA states due to its low signal-to-noise ratio limited its discriminative ability.[4,48-50] The developed model's reconstruction errors achieved a more pronounced significant difference between active and inactive CA states regarding PRx. It may be that the model exploited additional CA information found in the ICP signal such as Mayer waves, which correlate with cerebral hemodynamics, and ICP pulse morphology, which contains

© Congress of Neurological Surgeons 2025. Unauthorized reproduction of this article is prohibited.

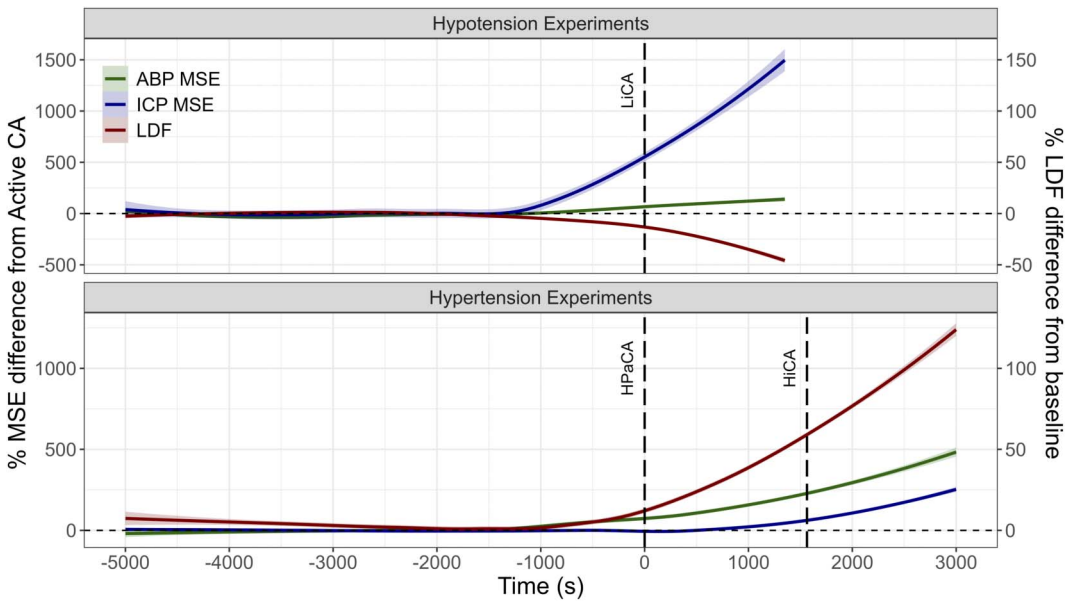


FIGURE 4. *Percentage change of ABP and ICP MSE and of percentage change of LDF from baseline over time visualized per piglet experimental condition. LiCA, HPaCA and HiCA reflect the low inactive CA, hypertensive high partially active CA, and high inactive CA, respectively. The onset of LiCA and HPaCA was centered as time point 0 to combine the data of all piglets within the experimental condition. Data points were smoothed using a locally weighted nonparametric regression with an α of 0.75 and visualized with their 95% CIs. ABP, arterial blood pressure; active CA, active cerebrovascular autoregulation; HiCA, high inactive CA; HPaCA, hypertensive high partially active CA; ICP, intracranial pressure; ICP, intracranial pressure; LDF, laser Doppler flow; LiCA, hypotensive Low inactive CA; MSE, mean squared reconstruction error.*

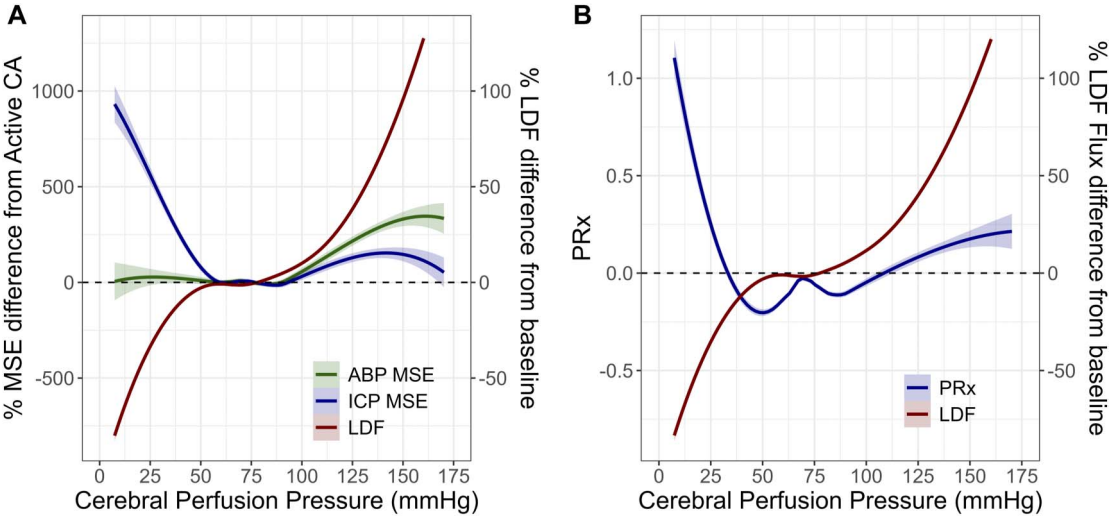


FIGURE 5. *Percentage change of ABP and ICP MSE and PRx over CPP.* **A**, *ABP and ICP MSE percentage difference from active CA.* **B**, *PRx plotted against corresponding CPP values. Both graphics were visualized with LDF percentage difference from baseline depicted on the right y-axis. Data points were smoothed using a locally weighted non parametric regression with an α of 0.75 and visualized with their 95% CIs. ABP, arterial blood pressure; active CA, active cerebrovascular autoregulation; CPP, cerebral perfusion pressure; ICP, intracranial pressure; LDF, laser Doppler flow; MSE, mean squared reconstruction error; PRx, pressure reactivity index.*

© Congress of Neurological Surgeons 2025. Unauthorized reproduction of this article is prohibited.

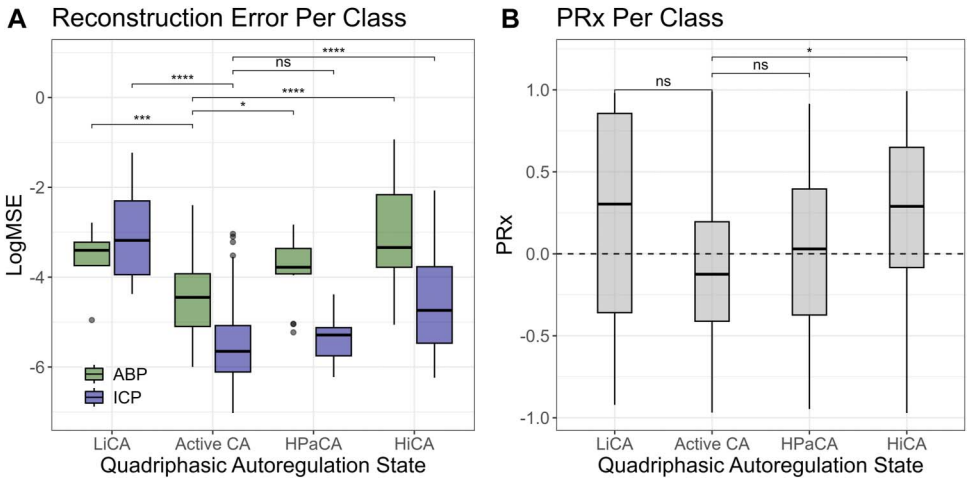


FIGURE 6. *Model test prediction error and PRx distribution along quadriphasic CA states. LiCA, active CA, HPaCA, and HiCA correspond to the hypotensive inactive CA, active CA, hypertensive partially active CA, and hypertensive inactive CA states, respectively.* **A**, *Model test LogMSE per quadriphasic CA state. LogMSE was computed per reconstructed concurrent ABP and ICP segment of 300 seconds. A lower LogMSE reflects better reconstruction performance.* **B**, *PRx distribution along CA state. ABP and ICP data were modeled with a LMM with a main effect of variable, CA state, and their interaction as fixed effect. PRx data were modeled with a LMM with CA state as fixed effect. The fixed effect CA states were subsequently contrasted and corrected for multiple comparisons with Holm-Bonferroni correction. Note, that for the ABP-ICP model, the CA states contrasts were conditioned on variable. ****P < .0001; ***P < .001; **P < .01; *P < .05; ns, not significant. ABP, arterial blood pressure; active CA, active cerebrovascular autoregulation; HiCA, high inactive CA; HPaCA, hypertensive high partially active CA; ICP, intracranial pressure; LiCA, hypotensive low inactive CA; LogMSE, log mean squared reconstruction error; LMM, linear mixed effects model; ns, not significant; PRx, pressure reactivity index.*

information on cerebrovascular hemodynamics and cerebrospinal pressure-volume compensation, and their relation to ABP signal components.[21-28]

ABP and ICP reconstruction error increases followed the corresponding percentage difference from baseline LDF closely when plotted against time and CPP. Strikingly, ABP and ICP reconstruction errors increased concurrently over time and CPP when LDF started to deviate from baseline, which happened before the time points indicative of the transition from active CA to (partially) inactive CA.[6] The latter observation reflects an often overlooked drawback by deriving CA labels from the Lassen or quadriphasic CA curve. The optimal least squares fit–derived breakpoint(s) does not necessarily reflect the actual deflection point from stable LDF in time or CPP (cf. Figure 4). That ICP and ABP reconstruction errors responded immediately to LDF deviation means that the model was able to overcome this limitation and generalize over ABP and ICP input which reflected a stable LDF. PRx transitioned to positive correlations with a noticeable delay regarding LDF deviation from baseline over CPP.

Limitations

The presented study did encompass several limitations. The animal model data set used to train, validate, and test the model was relatively small (n = 16). However, cross-validation showed that the obtained results were robust because they generalized over 8 subsets of unique piglet train, validation, and test data sets. This is a healthy physiology animal model, and hence, pathophysiological situations that dynamically impair CA were not part of the generated data and thus were not analyzed. The animal model used concerned piglets that were aged 6 weeks; however, their cerebral and cardiovascular physiology is akin to humans.[6,8] Physiology studies confirmed that 6-week-old piglets have the capacity to actively vasodilate or vasoconstriction pial arterioles in response to changes in CPP, and show a robust CA capacity.[6,8,51-53]

Future Perspectives

Some crucial steps need to be taken to further develop the present proof-of-concept into a validated CA monitor. First, more experimental data, akin to the used data set, need to be gathered, with additional alterations (eg, CO_2, ICP). Second, an experimental severe TBI data set with dynamic CA impairment needs to be developed to validate the proof-of-concept. Third, a retrospective exploration followed by a prospective validation study of the outlined method in human TBI patients is needed. Finally, the equivalent method can be used to model an inactive CA representation, which could work in conjunction with the active CA model to further improve discriminative performance.

© Congress of Neurological Surgeons 2025. Unauthorized reproduction of this article is prohibited.

CONCLUSION

The presented proof-of-concept study showed that the proposed novel method and model works as intended and can develop into a state-of-the-art dynamic CA monitor. It was sufficient to use 300-second segments of ABP and ICP sampled at 20 Hz to directly derive changes in CBF.

Code and Data availability

The code and data that support the findings of this study are available from the corresponding author on reasonable request.

Funding

This study did not receive any funding or financial support.

Disclosures

The method described in the present work is pending a European patent application (EP24169467.8). Bavo Kempen is funded by a PhD fellowship strategic basic research from the Foundation for Scientific Research Flanders (FWO) (1S12523N) and was funded through a Research Chair on Brain Trauma awarded by the Laly Foundation to Bart Depreitere. Maarten De Vos is funded by the Flemish Government, Belgium (AI Research Program); FWO SB Project (S003524N); FWO Research Projects (G0C9623N, G0D8321N). Bart Depreitere receives grant funding from FWO and Laly Foundation. Veerle De Sloovere received funding from KOOR: clinical research fund from the University Hospitals Leuven Belgium. The other authors have no personal, financial, or institutional interest in any of the drugs, materials, or devices described in this article.

REFERENCES

1. Lassen NA. Cerebral blood flow and oxygen consumption in man. *Physiol Rev.* 1959;39(2):183-238.
2. Aaslid R, Lindegaard KF, Sorteberg W, Nornes H. Cerebral autoregulation dynamics in humans. *Stroke.* 1989;20(1):45-52.
3. Toth P, Szarka N, Farkas E, et al. Traumatic brain injury-induced autoregulatory dysfunction and spreading depression-related neurovascular uncoupling: pathomechanisms, perspectives, and therapeutic implications. *Am J Physiol Heart Circ Physiol.* 2016;311(5):H1118-H1131.
4. Depreitere B, Citerio G, Smith M, et al. Cerebrovascular autoregulation monitoring in the management of adult severe traumatic brain injury: a Delphi consensus of clinicians. *Neurocrit Care.* 2021;34(3):731-738.
5. Meng L, Gelb AW. Regulation of cerebral autoregulation by carbon dioxide. *Anesthesiology.* 2015;122(1):196-205.
6. Klein SP, De Sloovere V, Meyfroidt G, Depreitere B. Differential hemodynamic response of pial arterioles contributes to a quadriphasic cerebral autoregulation physiology. *J Am Heart Assoc.* 2022;11(1):e022943.
7. Silverman A, Petersen NH. Physiology, cerebral autoregulation. StatPearls. StatPearls Publishing; 2023.
8. Klein SP, De Sloovere V, Meyfroidt G, Depreitere B. Autoregulation assessment by direct visualisation of pial arterial blood flow in the piglet brain. *Sci Rep.* 2019;9(1):13333.
9. Drummond JC. The lower limit of autoregulation: time to revise our thinking? *Anesthesiology.* 1997;86(6):1431-1433.
10. Donnelly J, Budohoski KP, Smielewski P, Czosnyka M. Regulation of the cerebral circulation: bedside assessment and clinical implications. *Crit Care.* 2016;20(1):129.
11. Kahl U, Yu Y, Nierhaus A, et al. Cerebrovascular autoregulation and arterial carbon dioxide in patients with acute respiratory distress syndrome: a prospective observational cohort study. *Ann Intensive Care.* 2021;11(1):47.
12. Muizelaar JP, Ward JD, Marmarou A, Newlon PG, Wachi A. Cerebral blood flow and metabolism in severely head-injured children. Part 2: autoregulation. *J Neurosurg.* 1989;71(1):72-76.
13. Czosnyka M, Smielewski P, Piechnik S, Steiner LA, Pickard JD. Cerebral autoregulation following head injury. *J Neurosurg.* 2001;95(5):756-763.
14. Immink RV, van Montfrans GA, Stam J, Karemaker JM, Diamant M, van Lieshout JJ. Dynamic cerebral autoregulation in acute lacunar and middle cerebral artery territory ischemic stroke. *Stroke.* 2005;36(12):2595-2600.
15. Claassen JAHR, Zhang R. Cerebral autoregulation in Alzheimer's disease. *J Cereb Blood Flow Metab.* 2011;31(7):1572-1577.
16. Budohoski KP, Czosnyka M, Smielewski P, et al. Monitoring cerebral autoregulation after subarachnoid hemorrhage. *Acta Neurochir Suppl.* 2016;122:199-203.
17. Zeiler FA, Donnelly J, Cardim D, Menon DK, Smielewski P, Czosnyka M. ICP versus laser Doppler cerebrovascular reactivity indices to assess brain autoregulatory capacity. *Neurocrit Care* 2018;28(2):194-202.
18. Czosnyka M, Smielewski P, Kirkpatrick P, Laing RJ, Menon D, Pickard JD. Continuous assessment of the cerebral vasomotor reactivity in head injury. *Neurosurgery.* 1997;41(1):11-19.
19. Fraser CD, Brady KM, Rhee CJ, et al. The frequency response of cerebral autoregulation. *J Appl Physiol.* 2013;115(1):52-56.
20. Czosnyka M, Czosnyka Z, Smielewski P. Pressure reactivity index: journey through the past 20 years. *Acta Neurochir.* 2017;159(11):2063-2065.
21. Dai H, Jia X, Pahren L, Lee J, Foreman B. Intracranial pressure monitoring signals after traumatic brain injury: a narrative overview and conceptual data science framework. *Front Neurol.* 2020;11:959.
22. Julien C. The enigma of Mayer waves: facts and models. *Cardiovasc Res.* 2006;70(1):12-21.
23. Whittaker JR, Driver ID, Venzi M, Bright MG, Murphy K. Cerebral autoregulation evidenced by synchronized low frequency oscillations in blood pressure and resting-state fMRI. *Front Neurosci.* 2019;13:433.
24. Whittaker JR, Driver ID, Venzi M, Bright MG, Murphy K. Corrigendum: cerebral autoregulation evidenced by synchronized low frequency oscillations in blood pressure and resting-state fMRI. *Front Neurosci.* 2020;14:544.
25. Julien C. An update on the enigma of Mayer waves. *Cardiovasc Res.* 2020;116(14):e210-e211.
26. Ellis T, McNames J, Goldstein B. Residual pulse morphology visualization and analysis in pressure signals. In: 2005 IEEE Engineering in Medicine and Biology 27th Annual Conference; 2005:3966-3969.
27. Ellis T, McNames J, Aboy M. Pulse morphology visualization and analysis with applications in cardiovascular pressure signals. *IEEE Trans Biomed Eng.* 2007;54(9):1552-1559.
28. Czosnyka M, Czosnyka Z. Origin of intracranial pressure pulse waveform. *Acta Neurochir.* 2020;162(8):1815-1817.
29. Wu M, Zhang W, Guo Z, et al. Separation of normal and impaired dynamic cerebral autoregulation using deep embedded clustering: a proof-of-concept study. *Physiol Meas.* 2021;42(7):074002.
30. Chauhan S, Vig L. Anomaly detection in ECG time signals via deep long short-term memory networks. In: 2015 IEEE International Conference on Data Science and Advanced Analytics (DSAA); 2015:1-7.
31. Guo Y, Liao W, Wang Q, Yu L, Ji T, Li P. Multidimensional time series anomaly detection: a GRU-based Gaussian mixture variational autoencoder approach. Proceedings of the 10th Asian Conference on Machine Learning. 2018;95:97-112.
32. Li D, Chen D, Jin B, Shi L, Goh J, Ng SK. MAD-GAN: multivariate anomaly detection for time series data with generative adversarial networks. Lecture Notes in Computer Science 2019:703-716. Accessed February 23, 2021. https://arxiv.org/abs/1901.04997
33. Pol AA, Berger V, Cerminara G, Germain C, Pierini M. Anomaly detection with conditional variational autoencoders. arXiv:201005531 [hep-ex]; 2020. Accessed February 15, 2021. https://arxiv.org/abs/2010.05531
34. Seeuws N, De Vos M, Bertrand A. Electrocardiogram quality assessment using unsupervised deep learning. *IEEE Trans Biomed Eng.* 2022;69(2):882-893.
35. Wu H, Hu T, Liu Y, Zhou H, Wang J, Long M. TimesNet: temporal 2D-variation modeling for general time series analysis; 2023. Accessed March 3, 2023. https://arxiv.org/abs/2210.02186
36. Chandola V, Banerjee A, Kumar V. Anomaly detection: a survey. *ACM Comput Surv.* 2009;41(3):1-15.

© Congress of Neurological Surgeons 2025. Unauthorized reproduction of this article is prohibited.

37. HDF5, the new ICM+ data format. Cambridge Enterprise ICM+. https://icmplus.neurosurg.cam.ac.uk/home/icm-features/hdf5-new-icm-data-format/
38. Nyquist H. Certain topics in telegraph transmission theory. *Trans Am Inst Electr Eng.* 1928;47(2):617-644.
39. Shannon CE. Communication in the presence of noise. *Proc IRE.* 1949;37(1):10-21.
40. Van Rossum G, Drake FL. Python 3 reference manual. *CreateSpace.* 2009.
41. Paszke A, Gross S, Massa F, et al. PyTorch: an imperative style, high-performance deep learning library. In: *Advances in Neural Information Processing Systems*, Vol 32. Curran Associates, Inc; 2019.
42. Singmann H, Kellen D. An introduction to mixed models for experimental psychology. In: Spieler D Schumacher E, eds. *New Methods in Cognitive Psychology*, 1st edn. Routledge; 2019:4-31.
43. Holm S. A simple sequentially rejective multiple test procedure. *Scand J Stat.* 1979;6(2):65-70.
44. R Core Team. *R: A Language and Environment for Statistical Computing*. R Foundation for Statistical Computing; 2016.
45. Wickham H, Averick M, Bryan J, et al. Welcome to the Tidyverse. *J Open Source Softw.* 2019;4(43):1686.
46. Bates D, Mächler M, Bolker B, Walker S. Fitting linear mixed-effects models using Lme4. *J Stat Softw.* 2015;67(1):1-48.
47. Niu Z, Yu K, Wu X. LSTM-based VAE-GAN for time-series anomaly detection. *Sensors.* 2020;20(13):3738.
48. Willie CK, Tzeng YC, Fisher JA, Ainslie PN. Integrative regulation of human brain blood flow. *J Physiol.* 2014;592(5):841-859.
49. Zeiler FA, Donnelly J, Menon DK, et al. Continuous autoregulatory indices derived from multi-modal monitoring: each one is not like the other. *J Neurotrauma.* 2017;34(22):3070-3080.
50. Howells T, Johnson U, McKelvey T, Enblad P. An optimal frequency range for assessing the pressure reactivity index in patients with traumatic brain injury. *J Clin Monit Comput.* 2015;29(1):97-105.
51. Brady KM, Lee JK, Kibler KK, Easley RB, Koehler RC, Shaffner DH. Continuous measurement of autoregulation by spontaneous fluctuations in cerebral perfusion pressure: comparison of 3 methods. *Stroke.* 2008;39(9):2531-2537.
52. Brady KM, Mytar JO, Kibler KK, et al. Noninvasive autoregulation monitoring with and without intracranial pressure in the naïve piglet brain. *Anesth Analgesia.* 2010;111(1):191-195.
53. Zeiler FA, Lee JK, Smielewski P, Czosnyka M, Brady K. Validation of intracranial pressure-derived cerebrovascular reactivity indices against the lower limit of autoregulation, Part II: experimental model of arterial hypotension. *J Neurotrauma.* 2018;35(23):2812-2819.

Acknowledgments

We would like to acknowledge Sofie Dietvorst, MD PhD, Clinical fellow at the Alder Hey Children's Hospital, Liverpool, United Kingdom, for the advice given throughout this project. The resources and services used in this work were provided by the VSC (Flemish Supercomputer Center), funded by the Research Foundation - Flanders (FWO) and the Flemish Government. Author Contribution: Bavo Kempen: Conceptualization, Methodology, Software, Formal analysis, Investigation, Data Curation, Writing—Original Draft, Writing—Review & Editing, Visualization, Funding acquisition. Samuel Klein: Resources. Veerle De Sloovere: Resources. Maarten De Vos: Conceptualization, Methodology, Writing—Original Draft, Writing—Review & Editing, Supervision. Bart Depreitere: Conceptualization, Methodology, Writing—Original Draft, Writing—Review & Editing, Supervision, Project administration, Funding acquisition.

Supplemental digital content *is available for this article at neurosurgery-online.com.*

Supplemental Digital Content 1. **Figure 1**. Hypotension and hypertension was nonpharmacologically induced in twenty 6-week-old male piglets (domestic swine) by gradually inflating a balloon catheter in the inferior vena cava or abdominal aorta, respectively. This illustration was kindly provided by Dr Gabriel Montaldo and Dr Alan Urban, Urban Laboratory, Neuro-Electronics Research Flanders (NERF), VIB, KU-LEUVEN.

Supplemental Digital Content 2. **Algorithm 1**. Procedure model training and evaluation. The unique piglets present in the complete data set were randomly assigned to a training (n = 12), validation (n = 2), and test (n = 2) data set, stratified on arterial blood pressure (ABP) manipulation using 4-fold nested cross-validation (cv_training_dataset, cv_validation_dataset, cv_test_dataset). Training and validation data sets comprised active cerebrovascular autoregulation (CA) data, while test data set consisted of low ABP inactive CA (LiCA), active CA, high ABP partially active CA (HPaCA), and high ABP inactive CA (HiCA). The training data set was used to globally standardize the training, validation, and test data sets to ensure that loss values between ABP and ICP were on the same scale (cf. step 2 and 7). To ensure that each individual time series (ABP and ICP) was standard normal distributed and thus invariant to absolute or relative differences in ABP and ICP values, a second standardization step took place and they were standardized on their own mean and standard deviation (cf. step 3.2.1 and 3.2.3). He initialization was used to initialize model parameters θ, an Adaptive Moment Estimation optimizer was used with learning rate 0.0001, number of epochs "T" = 100, batch size "B" = 32, early stopping manifested if validation loss did not decrease for 5 consecutive epochs.

Supplemental Digital Content 3. **Equation 1**. Linear mixed effects model (LMM) to assess effect of cerebrovascular autoregulation (CA) state on the pressure reactivity index (PRx). The equation describes the maximal random effects structure justified by the experimental design. Afterward, the LMM was simplified to a fixed main effect for CA state and a by-piglet random intercept and slope for CA state with an uncorrelated random effects structure. Pairwise contrasts were computed on the main effect of CA state, using Holm-Bonferroni correction for multiple comparisons: low ABP inactive CA (LiCA) state, high ABP partially active CA (HPaCA) state, and high ABP inactive CA (HiCA) state.

Supplemental Digital Content 4. **Equation 2**. Linear mixed effects model (LMM) to assess effect of cerebrovascular autoregulation (CA) state and reconstructed variable on the reconstruction error. The log mean squared error (LogMSE) reflects the arterial blood pressure (ABP) and intracranial pressure (ICP) reconstruction errors. A main effect of CA state, variable (ABP, ICP), and their interaction was considered and denoted in the equation with the maximal random effects structure justified by the experimental design. The final LMM was simplified to a main effect of CA state, variable (ABP, ICP), and their interaction, and a by-piglet, cross-validation fold random intercepts and slopes for variable with an uncorrelated random effects structure. Pairwise contrasts were computed on the interaction effect of CA state and variable by conditioning on the variable to derive the (non)significant differences between CA states per variable, using Holm-Bonferroni correction for multiple comparisons: low ABP inactive CA (LiCA) state, high ABP partially active CA (HPaCA) state, and high ABP inactive CA (HiCA) state.

Supplemental Digital Content 5. **Figure 2**. Original arterial blood pressure (ABP) and intracranial pressure (ICP) input traces (blue) and respective reconstructions (red) from the test data set active CA. The left and right figures per row concern concurrent standardized ABP and ICP traces, respectively. Each ABP and ICP trace is provided with a 10-second zoom window derived from the 300-second input-reconstruction segments.

Supplemental Digital Content 6. **Figure 3**. Original arterial blood pressure (ABP) and intracranial pressure (ICP) input traces (blue) and respective reconstructions (red) from the test data set: low ABP inactive cerebrovascular autoregulation (LiCA). The left and right figures per row concern concurrent standardized ABP and ICP traces, respectively. Each ABP and ICP trace is provided with a 10-second zoom window derived from the 300-second input-reconstruction segments.

Supplemental Digital Content 7. **Figure 4**. Original arterial blood pressure (ABP) and intracranial pressure (ICP) input traces (blue) and respective reconstructions (red) from the test data set: high ABP partially active cerebrovascular autoregulation (HPaCA). The left and right figures per row concern concurrent standardized ABP and ICP traces, respectively. Each ABP and ICP trace is provided with a 10-second zoom window derived from the 300-seconds input-reconstruction segments.

© Congress of Neurological Surgeons 2025. Unauthorized reproduction of this article is prohibited.

Supplemental Digital Content 8. **Figure 5**. Original arterial blood pressure (ABP) and intracranial pressure (ICP) input traces (blue) and respective reconstructions (red) from the test data set: high ABP inactive cerebrovascular autoregulation (HiCA). The left and right figures per row concern concurrent standardized ABP and ICP traces, respectively. Each ABP and ICP trace is provided with a 10-second zoom window derived from the 300-second input-reconstruction segments.

Supplemental Digital Content 9. **Table 1**. Log mean squared error (LogMSE) contrasts over cerebrovascular autoregulation (CA) states, conditioned on variable. First, a linear mixed effect model was fit with main effect of CA state, variable (ABP, ICP), and their interaction (cf. Supplementary equation 2) and LogMSE as dependent variable. To determine whether reconstruction error (LogMSE) significantly increased under inactive CA states regarding the active CA state for each variable (ABP, ICP) separately, pairwise contrasts of the CA state and variable interaction, conditioned on variable, were evaluated and adjusted with the Holm-Bonferroni correction. The asymptotic *z*-test was used to assess pairwise contrasts due to large number of data points available (infinite degrees of freedom). Here, the authors were mainly interested in the contrasts of active CA with the inactive CA states (cf. Figure 6).

Supplemental Digital Content 10. **Table 2**. Pressure-reactivity index (PRx) contrasts over cerebrovascular autoregulation (CA) states. First, a linear mixed effect model was fit with main effect of CA state (cf. Supplementary Equation 1) and PRx as dependent variable. To determine whether PRx significantly increased under inactive CA states regarding the active CA state, pairwise contrasts of the CA state were performed and adjusted with the Holm-Bonferroni correction. The asymptotic *z*-test was used to assess pairwise contrasts due to large number of data points available (infinite degrees of freedom). Here, the authors were mainly interested in the contrasts of active CA with the inactive CA states (cf. Figure 6).

© Congress of Neurological Surgeons 2025. Unauthorized reproduction of this article is prohibited.